

Structural and Magnetic Studies of Thermally Treated NiFe₂O₄ Nanoparticles



SURAJIT GHOSH, PRAYAS CHANDRA PATEL, DEBRAJ GANGOPADHYAY, POORNIMA SHARMA, RANJAN K. SINGH, and P.C. SRIVASTAVA

The heat treatment of nanoparticles can have a direct effect on their particle sizes, which, in turn, can influence many of their structural and magnetic properties. Here, we report the effect of sintering temperature on the chemically synthesized high-quality NiFe₂O₄ nanoparticles. The structural studies show the formation of pure NiFe₂O₄ nanoparticles with the space group $Fd\bar{3}m$. The inverse spinel structure was also confirmed from the lattice vibrations analyzed from Raman and Fourier transform infrared spectroscopy (FTIR) spectra. The presence of strong exchange interactions was detected from the temperature-dependent magnetization study. Moreover, at higher sintering temperatures, the grain growth due to fusion of several smaller particles by coalescing their surfaces enhances the crystallinity and its magnetocrystalline anisotropy. Coercivity and saturation magnetization were found to depend significantly on the sintering temperature, which was understood in the realm of the formation of single-domain-like structure and change in magnetocrystalline anisotropy at higher sintering temperatures.

DOI: 10.1007/s11661-017-4344-y

© The Minerals, Metals & Materials Society and ASM International 2017

I. INTRODUCTION

IN recent times, magnetization of the ferromagnetic materials has evolved as a fundamental quantity resulting in significant growth in the synthesis and study of magnetic nanoparticles, as they show interesting properties that are different from their bulk counterparts due to their surface effect and quantum confinement effects.^[1] Among the magnetic nanoparticle spinel, ferrites have gained much attention due to their interesting electrical, magnetic, optical, and catalytic properties, which make them a potential candidate^[2] to be applied in various fields, such as magnetic storage systems,^[3] magnetic resonance imaging,^[4] photomagnetic devices,^[5] ferrofluids, radar absorbing coating,^[6] drug delivery,^[7] and gas sensors.^[8] NiFe₂O₄ is widely known for its high electromagnetic performance, high coercivity, moderate saturation magnetization,^[1,8] good mechanical hardness, and excellent chemical stability,^[9] which makes it a promising material for the foresaid

applications. Like most ferrites, NiFe₂O₄ also has an inverse spinel structure^[8] in which there exists face-centered-cubic (fcc) lattice of O²⁻ ions and Fe³⁺ ions distributed over tetrahedral (A) and octahedral (B) sites equally and Ni²⁺ ions located in octahedral sites only. In the case of inverse spinel, magnetic moments of the A and B sites are aligned antiparallel to each other, resulting in the cancellation of the moment for Fe³⁺; thus, it forms a collinear ferromagnetic ordering with Curie temperature ~870 K (~597 °C).^[8]

Depending on the cation distribution between octahedral and tetrahedral sites, spinel structure can be of “normal,” “inverse,” or “mixed” form and any changes in cation distribution can lead to switching among them.^[8] Thus, the synthesis route that influences the cation distribution as well as composition, purity, and microstructure of the nanoparticles plays an important role in controlling the properties of the synthesized nanoparticles. Various synthesis techniques have been applied so far to synthesize nanoparticles of NiFe₂O₄ of desired properties, such as microemulsion synthesis,^[1] hydrothermal synthesis,^[10] sol-gel,^[11] coprecipitation,^[12] and combustion method.^[13] The coprecipitation method, being a simple and low-cost technique, can be significant in preparing ferrite nanoparticles, as it provides easy control on various synthesis parameters. Moreover, many properties, such as particle size, stoichiometry, and structural phase of the nanoparticles, can also be controlled by sintering synthesized samples at elevated temperatures.^[12]

SURAJIT GHOSH, PRAYAS CHANDRA PATEL, DEBRAJ GANGOPADHYAY, POORNIMA SHARMA, RANJAN K. SINGH, and P.C. SRIVASTAVA are with the Department of Physics, Institute of Science, Banaras Hindu University, Varanasi, U.P. 221005, India. Contact e-mail: pcsrivastava50@gmail.com

Manuscript submitted May 1, 2017.

Article published online September 26, 2017

In this context, we have employed a coprecipitation method followed by sintering the as-prepared samples at different elevated temperatures to synthesize NiFe₂O₄ nanoparticles and investigated the effect of heat treatment on their structure, lattice vibration, and magnetic properties. For understanding of the structural evolution of the synthesized samples with the heat treatment and to gather information about the phases present and their dimensions, we have carried out X-ray diffraction (XRD), scanning electron microscopy (SEM), transmission electron microscopy (TEM), Fourier transform infrared spectroscopy (FTIR), and Raman measurements. The results from the structural studies have been found to be very useful in understanding the magnetic behavior of the nanosized particles studied from the ZFC–FC magnetization and M–H characteristics.

II. EXPERIMENTAL DETAILS

The nickel ferrite nanoparticles were synthesized by the coprecipitation method^[12] using analytical grade (more than 99 pct purity) Ni(NO₃)₂·6H₂O and Fe(NO₃)₃·9H₂O as the source of Ni²⁺ and Fe³⁺ ions, respectively, with double distilled water as the solvent. A 250-mL solution of 0.04 M Ni(NO₃)₂·6H₂O and 0.08 M Fe(NO₃)₃·9H₂O was prepared to keep Ni²⁺ and Fe³⁺ ions in proper stoichiometric ratio (1:2). 35.1 mL of 30 pct ammonia solution was added dropwise to the solution under vigorous stirring (600 rpm). The stirring was continued for 3 hours at room temperature to obtain homogeneous mixing. The orange precipitate so formed was filtered out and rinsed with distilled water several times to remove impurities and was dried in an electrical oven at 353 K (80 °C). The dried samples were ground in an agate mortar to obtain the powder samples, which were sintered at 673 K, 773 K, 873 K, 973 K, 1073 K, and 1273 K (400 °C, 500 °C, 600 °C, 700 °C, 800 °C, and 1000 °C) at 10⁻³ Torr pressure for 10 hours. The samples were allowed to cool naturally and were taken for further analysis. The samples sintered at 673 K, 773 K, 873 K, 973 K, 1073 K, and 1273 K (400 °C, 500 °C, 600 °C, 700 °C, 800 °C, and 1000 °C) are named NFO_400, NFO_500, NFO_600, NFO_700, NFO_800, and NFO_1000 respectively.

Structural analysis of the powder samples was done from the XRD diffractograms obtained with an “X’PERT PRO PANALYTICAL” diffractometer using Cu K_α radiation ($\lambda = 1.54060 \text{ \AA}$). A “QUANTA 200 F” scanning electron microscope and FEI TECNAI 20G² transmission electron microscope were used for the microstructural investigation. FTIR measurements were done with a SHIMADZU ‘IR-AFFINITY1’ spectrophotometer. Raman spectra were recorded using a 532-nm laser in a “RENISHAW” Raman spectrometer. Magnetic properties of the samples M–H (at room temperature) and M–T were recorded using a MICROSENCE, USA vibrating sample magnetometer and SQUID magnetometer from QUANTUM DESIGN, USA, respectively.

III. RESULTS AND DISCUSSION

A. Structural and Morphological Analysis

Structural analysis of the nickel ferrite nanoparticles (NFO_400, NFO_600, NFO_800, and NFO_1000) was done by recording the XRD pattern (shown in Figure 1). The diffraction peaks at $2\theta = 18.23, 30.10, 35.49, 37.16, 43.18, 53.65, 57.20, 62.84, 71.28, 74.46, 75.39,$ and 79.62 deg were indexed to the reflection planes 111, 220, 311, 222, 400, 422, 511, 440, 620, 533, 622, and 444 of NiFe₂O₄. The diffraction patterns match well with the standard JCPDS Card No. 862267. Since no other impurity peak corresponding to any secondary phase/compound could be detected, the formation of pure single-phase NiFe₂O₄ with an fcc structure with the space group $Fd\bar{3}m$ is confirmed. With the increase of sintering temperature, intensity of the diffraction peaks increases while full-width at half-maxima (FWHM) decreases, resulting in gradual sharpening of the peaks, which obviously indicates enhancement in the crystalline nature of the nanoparticles. Moreover, higher order diffraction peaks corresponding to 620, 533, 622, and 444 planes appear for the sample sintered above 873 K (600 °C), the intensity of which increases with the temperature. The lattice parameter was also calculated from the XRD data, and it shows little variation with the increase in temperature for samples sintered at 873 K to 1273 K (600 °C to 1000 °C). The values of a were found to be 8.322, 8.345, and 8.365 Å for NFO_600, NFO_800, and NFO_1000, respectively, which were consistent with the standard JCPDS data. The increase in the lattice parameter with the increase in the sintering temperature can be understood as thermal expansion of the lattice.

The average crystallite size was determined from the FWHM using the well-known Debye–Scherrer relation, $D = 0.89\lambda/(\beta \cos \theta)$, where D is the crystallite size, λ is the wavelength of the X-ray used (Cu K_α = 1.5406 Å), β is the FWHM, and θ is the Bragg angle. The average

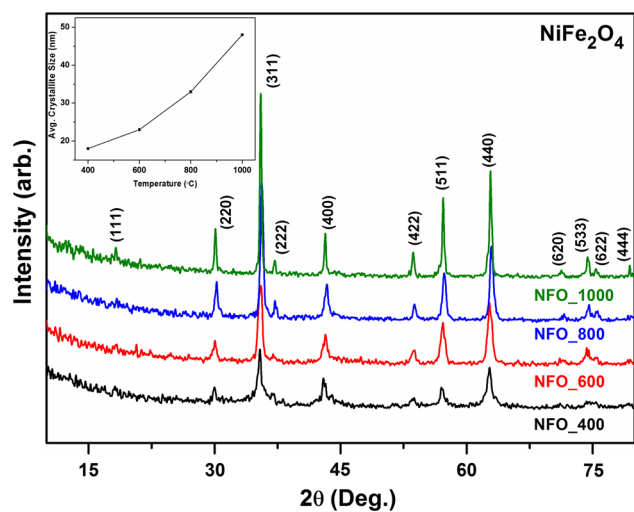


Fig. 1—XRD patterns of NiFe₂O₄ nanoparticles. Inset shows the variation of crystallite size with sintering temperature.

crystallite sizes were found to be ~18, 23, 31, and 37 nm for NFO_400, NFO_600, NFO_800, and NFO_1000, respectively. Thus, the average crystallite size was found to be increasing almost linearly with the sintering temperature (inset of Figure 1). An increase in the crystallite size with the rise of sintering temperature can be understood to be due to temperature-mediated self-aggregation of NiFe₂O₄ nanoparticles.^[14] Thus, among the samples, NFO_1000 shows better crystalline behavior with larger crystallite size.

The surface morphological features of the NiFe₂O₄ nanoparticles are shown in Figure 2 at a magnification of 20 μm. Particles of random shape and size, agglomerated in small clusters of size ranging from 1 to 10 μm, are distributed homogeneously throughout the samples. The agglomeration can be understood due to the high surface energy as a result of higher surface-to-volume ratio for smaller particles. A slight increase in the particle size can also be observed as the sintering temperature is raised above 873 K (600 °C). With increased particle size and crystallinity, some of the particles with smooth surfaces can be observed in NFO_800, while in NFO_1000, the smoothness becomes enhanced and sharp edges can be found. The morphological features, as observed in the SEM micrograph, are consistent with the XRD results that the particle size

and crystallinity of the samples increase with the increase in sintering temperature.

Figure 3 shows the transmission electron microscopy (TEM) images of NFO_600 and NFO_1000, showing the formation of highly crystalline particles with average sizes ~10 and ~20 nm, respectively, which are consistent with the average crystallite size, calculated from the Scherrer relation using XRD data. The results also indicate that the particles sintered at 600 and 1000 are uniform in morphology and are somewhat agglomerated in nature over the entire scan area. The rings observed in the selected area electron diffraction pattern (SAED) (inset) confirm the polycrystalline nature of the samples with a lattice parameter consistent with the fcc phase in the *Fd* $\bar{3}$ *m* space group of nickel ferrite, revealing no perceivable lattice distortion. The diffraction planes corresponding to the rings are consistent with the planes observed by XRD.

Thus, from the structural analysis, it can be concluded that sample NFO_1000 has a comparatively better crystalline nature. It has also been found that several particles fuse together to increase the particle size by coalescing their surfaces. This grain growth and enhancement in the particle size with sintering temperature has also been found in several ferrite systems, including cobalt ferrite,^[15] zinc ferrite,^[16] and nickel ferrite.^[17]

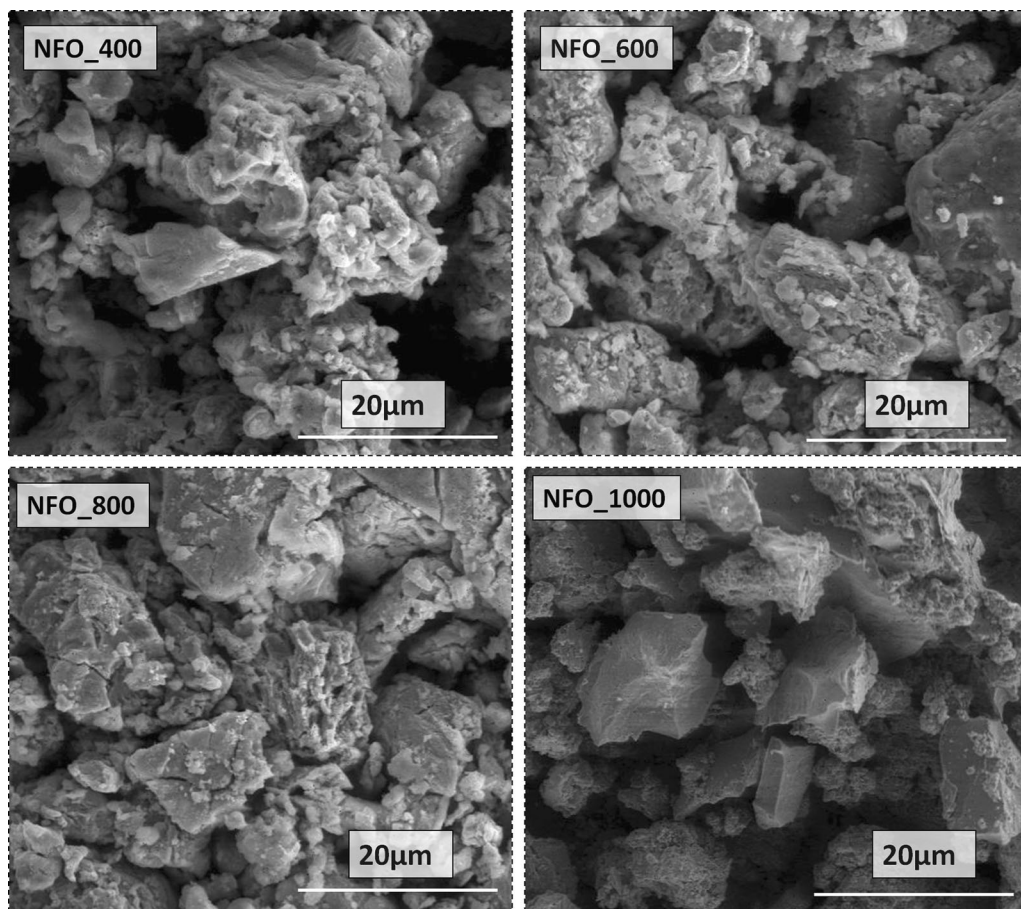


Fig. 2—SEM micrographs of NiFe₂O₄ nanoparticles.

B. Raman and FTIR Study

NiFe_2O_4 crystallizes into inverse spinel structure in which there are tetrahedral A sites (8A) occupied by half of the Fe^{3+} cations and octahedral B sites (16B) occupied by Ni^{2+} ions and the rest of the Fe^{3+} ions. There could be 13 modes, as predicted from the factor group analysis^[18] for the inverse spinel structure as follows:

$$A_{1g} + E_g + T_{1g} + 3T_{2g} + 2A_{2U} + 2E_U + 2T_{1U} + T_{2U}$$

In the spinel structure, out of these 13 normal modes, 5 modes are known to be Raman active ($A_{1g} + E_g + 3T_{2g}$) and 2 are IR active ($2T_{1U}$).

Figure 4 shows the Raman spectra of the samples NFO_500, NFO_600, NFO_700, NFO_800, and NFO_1000 in the range of 50 to 1250 cm^{-1} . The bands show a shoulder or doubletlike feature, a well-reported phenomenon for the spinel compounds.^[19] Peaks were observed at 700, 658 (shoulder), 575, 483, 332, and 211 cm^{-1} for all the samples, which correspond to the lattice vibrations of the ferrite.^[19-21] The most intense peak observed at 700 cm^{-1} is attributed to the A_{1g} mode of lattice vibration, which is a common feature of the Raman spectra of the inverse spinels.^[20] As this feature is observed irrespective of the chemical nature of the bivalent cation in any spinel ferrite, these bands must be assigned to the symmetric stretching of oxygen atoms along Fe-O bonds in tetrahedral coordination.^[20,22] The symmetric bending of oxygen ions with respect to the metal ions in tetrahedral coordination causes the E_g mode of vibration, which appeared at 332 cm^{-1} . One of the T_{2g} modes ($T_{2g}(1)$), observed at 220 cm^{-1} , corresponds to the tetrahedral sites (translational motions of tetrahedron together with the oxygen atoms), whereas the other two bands, $T_{2g}(2)$ at 483 cm^{-1} and $T_{2g}(3)$ at 575 cm^{-1} , correspond to the vibration of the octahedral group. $T_{2g}(2)$ appearing at the lower frequency is due to the asymmetric stretching of Fe-O or Ni-O, while $T_{2g}(3)$ is due to the asymmetric bending of the Fe-O or Ni-O. The broadening of the peaks can be understood to be due to the nanocrystalline nature of the ferrite samples. Sharpening and an increase in the intensity of the Raman peaks at 700, 497, and 211 cm^{-1} are observed

with the increase of the sintering temperature as the crystallinity of the samples are improved at higher sintering temperature, which is also evident from XRD analysis.

Further, Raman spectroscopy has been used widely to differentiate NiFe_2O_4 from other possible phases that may be formed during the preparation of NiFe_2O_4 in small amounts of impurity, such as $\alpha\text{-Fe}_2\text{O}_3$, $\gamma\text{-Fe}_2\text{O}_3$, and Fe_3O_4 , which have similar spinel structures and consequent similar XRD patterns.^[19,23,24] The Raman peaks for NiFe_2O_4 (Figure 4) are close to $\gamma\text{-Fe}_2\text{O}_3$, except for much stronger peaks at 1370 and 1580 cm^{-1} for $\gamma\text{-Fe}_2\text{O}_3$ than NiFe_2O_4 .^[19,24] Thus, the possibility of formation of $\gamma\text{-Fe}_2\text{O}_3$ during the heat-treatment process can be neglected, as very weak Raman absorption peaks are observed in the range 1300 to 1600 cm^{-1} (inset of Figure 4).

As mentioned earlier, the factor group analysis also predicted two IR active bands for the ferrite structures, which can be seen in the FT-IR spectra (Figure 5) measured in the range 400 to 2200 cm^{-1} . The bands at 592 and 418 cm^{-1} are the signature bands of NiFe_2O_4

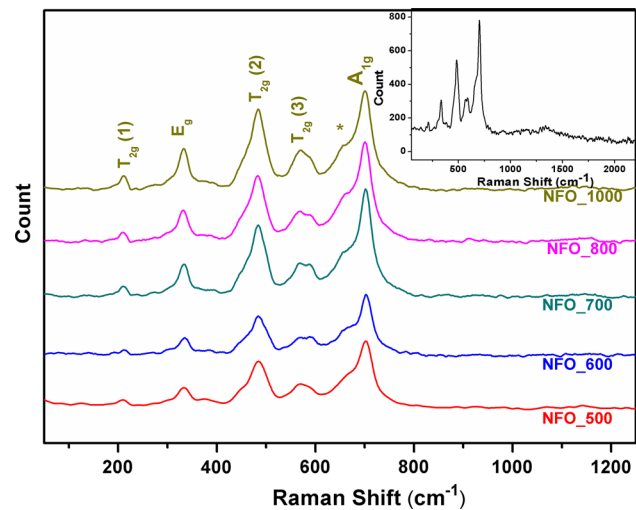


Fig. 4—Raman spectra of NiFe_2O_4 nanoparticles in the range 50 to 1250 nm. Inset shows Raman spectrum of NFO_1000 in the range 50 to 2250 nm.

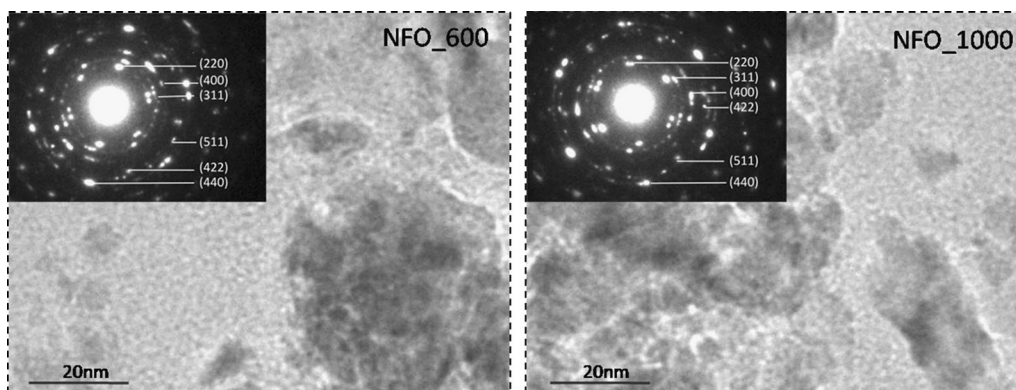


Fig. 3—TEM images of NFO_600 and NFO_1000. Inset shows corresponding SAED patterns.

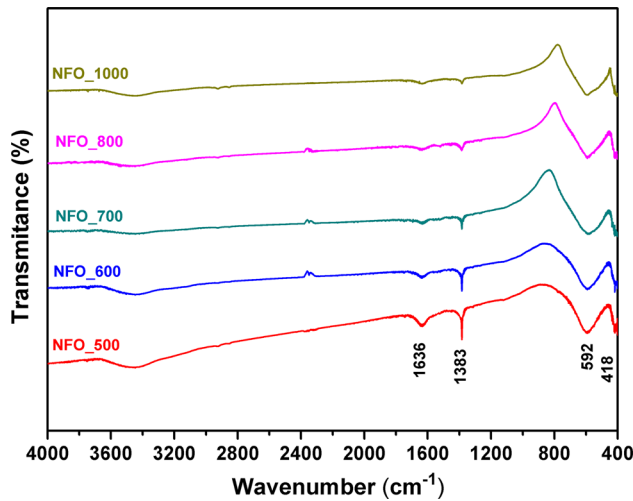


Fig. 5—FTIR spectra of NiFe₂O₄ nanoparticles.

phase corresponding to metal-oxygen bonds, *i.e.*, Fe-O vibrations and Ni-O stretching mode, respectively.^[22,25] Improved intensity of these bands with the sintering temperature shows better crystallinity of the NiFe₂O₄ nanoparticles. The band at 1383 cm⁻¹ is due to the antisymmetric NO₃⁻ stretching vibration that arises from the residual nitrate groups^[23] of the Ni(NO₃)₂ used as the precursor. The broad bands at 3400 and 1630 cm⁻¹ are attributed to the stretching modes of O-H group and H-O-H bending vibration, which show the presence of absorbed/adsorbed water.^[23] The weakening of intensity of these bands for the samples sintered at higher temperature indicates that the concentration of the residual nitrate and water becomes reduced at higher temperatures.

It can be concluded that the synthesized spinel ferrite was NiFe₂O₄, so the formation of other possible secondary phases, which have a similar XRD pattern as NiFe₂O₄, can be ruled out from Raman and FTIR studies. The inverse spinel structure of the ferrite, which was improved with higher sintering temperature, is also confirmed.

C. Magnetic Characterization

To study the magnetic properties of the synthesized samples, the temperature dependence of magnetization, zero field cooled (ZFC) and field cooled (FC), was measured with an applied low field of 0.1 kOe for NFO_400 and NFO_1000. To record the ZFC-FC magnetization curves, the samples were cooled to 10 K (-263 °C) in the presence of zero magnetic field $H = 0$ (ZFC) and $H = 100$ Oe (FC) and the magnetization was recorded on raising the temperature to 300 K (3 °C) in $H = 100$ Oe. The ZFC-FC curves, shown in Figure 6, are well apart, even at 300 K (3 °C), suggesting the blocking temperature (T_b) to be above room temperature. The diverging nature of the ZFC and FC curves below 300 K (3 °C) in both the samples indicates that the nanoparticles are not free but are strongly coupled by exchange interactions in this granular

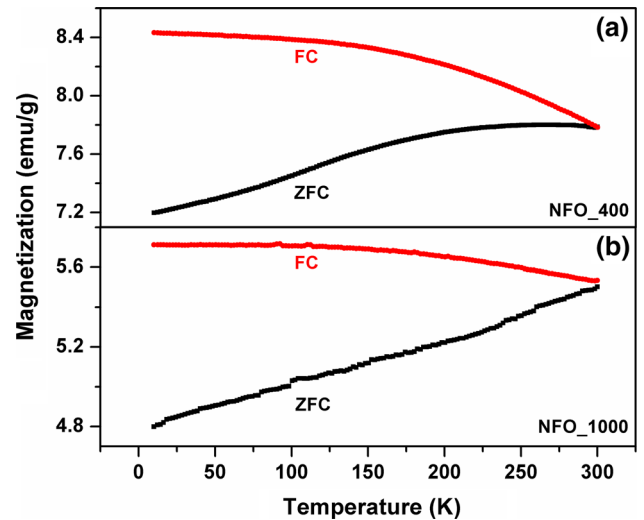


Fig. 6—Temperature dependence of magnetization with ZFC-FC process of (a) NFO_400 and (b) NFO_1000 measured at an applied field of 100 Oe.

system.^[26] Although the crystallite size was calculated to be much lower (~20 nm) from XRD data, from the SEM micrograph, it is found that the particles are agglomerated in nature, which might be the reason behind T_b being at a temperature higher than RT. With the increase of sintering temperature, the separation between ZFC and FC curves decreases, which means the interactions between particles become weaker. At low temperatures, the value of FC magnetization decreases with the increase of sintering temperature, which indicates that the rise in sintering temperature increases magnetic anisotropy as a result of enhancement in the crystallinity of the samples with higher sintering temperature, as observed from the structural study. It also indicates that the sintering temperature enhances the ferromagnetic moment, which can be due to the decrease in the exchange coupling.^[26,27]

Further, magnetization study of the samples NFO_400, NFO_600, NFO_800, and NFO_1000 from the M-H hysteresis loop (Figure 7) shows ferromagnetic behavior at room temperature. The coercivity (H_C) and saturation magnetization (M_S) of the samples, as observed from the hysteresis loop, have lower values in comparison to bulk NiFe₂O₄. With the increase of the sintering temperature, saturation magnetization is found to increase, which indicates that the magnetic interaction becomes stronger with the increase of sintering temperature. The saturation magnetization of S_1000 nearly approaches the value of bulk NiFe₂O₄ (56 emu g⁻¹).^[8,28] Inset (a) of Figure 7 shows the expanded view of the hysteresis loop around the origin (from -200 to 200 Oe). The variations of M_S and H_C as a function of sintering temperature are shown in the inset (b). Contrary to the M_S values, which increase with the sintering temperature, the coercivity shows (inset (b) of Figure 7) a decreasing nature. Enhanced saturation magnetization and denounced coercivity for the samples with higher sintering temperature can be elucidated on the basis of domain structure, critical size, magnetic

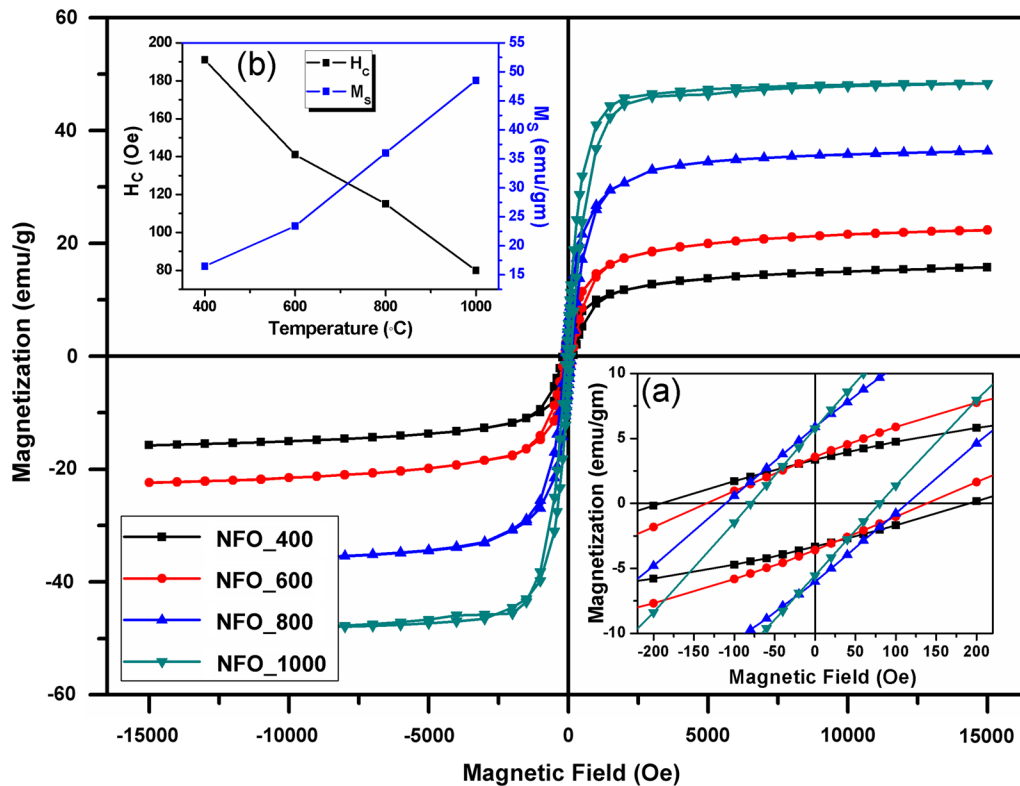


Fig. 7—M–H characteristics of NiFe_2O_4 nanoparticles measured at room temperature. Inset shows (a) expanded view of hysteresis loop and (b) variation of H_C and M_S with sintering temperature.

anisotropy, cation redistribution, surface spin, and formation of spin glass structures.^[29–32] The magnetic behavior of typical soft ferromagnetic materials, such as nickel ferrite, is significantly influenced by the synthesis route and particle size. Since the surface effects play a prominent role in the case of very small particles, the surface spin disorder affects the saturation magnetization in most of the magnetic nanoparticles, causing it to be much lower than the bulk value.^[33–35] Moreover, the static magnetic energy is reduced for relatively larger particles because of the formation of larger magnetic domains in such particles. At a certain radius, known as the critical radius (for nickel ferrite, this is ~ 100 nm), when the particle size approaches the size of the magnetic domain forming a single domain particle, coercive force decreases due to vanishing of the magnetization caused by the movement of domain walls.

Thus, from ZFC–FC and M–H characteristics, it seems that the surface of the nanoparticles is composed of some distorted or slanted spins and is likely to behave as an inactive or dead layer with inconsiderable magnetization that repels the core spins to align the field direction, resulting in exchange interaction. Consequently, the saturation magnetization decreases and coercivity increases for smaller sizes.^[36–38]

Moreover, the cation redistribution (interchanging of Ni and Fe ions of the tetrahedral and octahedral sites), which causes the structure of NiFe_2O_4 to transfer from an inverse spinel structure to a mixed spinel structure, can also influence the values of M_S and H_C with change in particle size.^[39] It is well known that the site inversion

takes place as the particle size is reduced. Thus, as the cation distribution in the samples depends significantly on the particle size, the observed magnetic properties of the samples can be understood in the realm of cation redistribution also. Moreover, from the study of Naseri *et al.*,^[17] it can be seen that pairs of similar spinel ferrite nanoparticles of the same particle size can have different saturation magnetization values and coercivity fields. This indicates that the magnetic properties of ferrites are very much dependent on the preparation method, which is also prominent from our study.

IV. CONCLUSIONS

Nickel ferrite nanoparticles were successfully synthesized *via* the coprecipitation method followed by sintering at different temperatures. Particles of 15 to 30 nm of fcc lattice of NiFe_2O_4 with phase group $Fd\bar{3}m$ were confirmed from the XRD pattern. From the SEM and TEM analysis, the particles were found to be of random shape and size. Particles of samples with higher sintering temperature were also found to be of better crystallinity. Different modes of lattice vibrations studied from Raman and FTIR spectroscopy confirmed the spinel structure of the ferrite. The residual water and nitrate group were found to get diminished as the sintering temperature was raised to 1273 K (1000 °C). Temperature-dependent magnetization study revealed the T_b of the samples to be above room temperature. The ferromagnetic properties characterized from ZFC–FC

measurement and M–H characteristics of the synthesized samples were found to be significantly influenced by the structural change due to the heat treatment, resulting in the increase of M_S and decrease in the H_C values. The observed changes in the magnetic properties were attributed to the change in magnetic anisotropy caused by the structural change and formation of single domain-like particles.

ACKNOWLEDGMENTS

The authors are thankful to Dr. Alok Banerjee, Scientist, UGC-DAE (Indore, India), for providing the SQUID facility and discussing the ZFC–FC results. The authors are also thankful to Mr. Debraj Gangopadhyay for helping with the Raman measurement and for discussing the Raman results.

REFERENCES

1. D.S. Mathew and R.S. Juang: *Chem. Eng. J.*, 2007, vol. 129, pp. 51–56.
2. B. Aslibeiki, P. Kameli, H. Salamati, M. Eshraghi, and T. Tahmasebi: *J. Magn. Magn. Mater.*, 2010, vol. 322, pp. 2929–34.
3. D.H. Han, H.L. Luo, and Z. Yang: *J. Magn. Magn. Mater.*, 1996, vol. 161, pp. 376–78.
4. C.H. Cunningham, T. Arai, P.C. Yang, M.V. McConnell, J.M. Pauly, and S.M. Connolly: *Magn. Reson. Med.*, 2005, vol. 53, pp. 999–1005.
5. A.K. Giri, K. Pellerin, W. Pongsaksawad, M. Sorescu, and S.A. Majetich: *IEEE Trans. Magn.*, 2000, vol. 36, pp. 3029–31.
6. R. Valenzuela: *Phys. Res. Int.*, 2012, vol. 2012, p. 591839.
7. Y.T. Jong, K.J. Sung, K.B. Geol, K. Nam, C.M. Haing, and L.J. Kyu: *Angew. Chem. Int. Ed.*, 2005, vol. 44, pp. 1068–95.
8. B.D. Cullity and S. Graham: *Introduction to Magnetic Materials*, Wiley, New York, NY, 2009.
9. A. Godman: *J. Mater. Eng. Perform.*, 1995, vol. 4, pp. 395–400.
10. J. Zhang, J. Shi, and M. Gong: *J. Solid State Chem.*, 2008, vol. 182, pp. 2135–40.
11. X.M. Liu, S.Y. Fu, and C.J. Huang: *J. Magn. Magn. Mater.*, 2004, vol. 281, pp. 234–39.
12. M.S. Niasari, F. Davar, and T. Mahmoudi: *Polyhedron*, 2009, vol. 28, pp. 1455–58.
13. M.A.F. Ramalho, L. Gama, S.G. Antonio, C.O. Paiva-Santos, E.J. Miola, R.H.G.A. Kiminami, and A.C.F.M. Costa: *J. Mater. Sci.*, 2007, vol. 42, pp. 3603–06.
14. W.Z. Wang, C.K. Xu, G.H. Wang, K.L. Liu, and C.L. Zheng: *Adv. Mater.*, 2002, vol. 14, pp. 837–40.
15. K. Maaz, A. Mumtaz, S.K. Hasanain, and A. Ceylan: *J. Magn. Magn. Mater.*, 2007, vol. 308, pp. 289–95.
16. M.K. Roy, B. Halder, and H.C. Verma: *Nanotechnology*, 2006, vol. 17, pp. 232–37.
17. M.G. Naseri, E.B. Saion, H.A. Ahangar, M. Hashim, and A.H. Shaari: *Powder Technol.*, 2011, vol. 212, pp. 80–88.
18. W.B. White and B.A. DeAngelis: *Spectrochim. Acta*, 1967, vol. 23A, pp. 985–95.
19. Z.H. Zhou, J.M. Xue, J. Wang, H.S.O. Chan, T. Yu, and Z.X. Shen: *J. Appl. Phys.*, 2002, vol. 91, pp. 6015–20.
20. J. Kreisel, G. Lucazeau, and H. Vincent: *J. Solid State Chem.*, 1998, vol. 137, pp. 127–37.
21. Y. Shi, J. Ding, Z.X. Shen, W.X. Sun, and L. Wang: *Solid State Commun.*, 2000, vol. 115, pp. 237–41.
22. A.A. Kamnev and M. Ristic: *J. Mol. Struct.*, 1997, vols. 408–409, pp. 301–04.
23. S. Yan, J. Geng, J. Chen, L. Yin, Y. Zhou, and E. Zhou: *J. Cryst. Growth*, 2004, vol. 262, pp. 415–19.
24. K.S.K. Varadwaj, M.K. Panigrahi, and J. Ghose: *J. Solid State Chem.*, 2004, vol. 177, pp. 4286–92.
25. T. Shimada, T. Tachibana, T. Nakagawa, and T.A. Yamamoto: *J. Alloys Compd.*, 2004, vol. 379, pp. 122–26.
26. Z.M. Tian, S.L. Yuan, S.Y. Yin, L. Liu, J.H. He, H.N. Duan, P. Li, and C.H. Wang: *Appl. Phys. Lett.*, 2008, vol. 93, pp. 222505–1–222505-3.
27. S.S. Starchikov, I.S. Lyubutin, C.R. Lin, Y.T. Tseng, K.O. Funtov, Y.L. Ogarkova, T.V. Dmitrieva, and A.G. Ivanova: *Phys. Chem. Chem. Phys.*, 2015, vol. 17, pp. 15829–36.
28. V. Sepelak, K. Tkacova, V.V. Boldyrev, S. Wibmann, and K.D. Becker: *Physica B*, 1997, vols. 234–236, pp. 617–19.
29. S. Chikazumi: *Physics of Magnetism*, Wiley, New York, 1959.
30. M. George, A.M. John, S.S. Nair, P.A. Joy, and M.R. Anantharaman: *J. Magn. Magn. Mater.*, 2006, vol. 302, pp. 190–95.
31. M.A. Gabal, Y.M.A. Angari, and M.W. Kadi: *Polyhedron*, 2011, vol. 30, pp. 1185–90.
32. Y. Cheng, Y. Zheng, Y. Wang, F. Bao, and Y. Qin: *J. Solid State Chem.*, 2005, vol. 178, pp. 2394–97.
33. S. Rana, R.S.M. Srivastava, M. Sorensson, and R.D.K. Misra: *Mater. Sci. Eng. B*, 2005, vol. 119, pp. 144–51.
34. R.D.K. Misra, S. Gubbala, A. Kale, and W.F. Egelhoff, Jr: *Mater. Sci. Eng. B*, 2004, vol. 111, pp. 164–70.
35. A.H. Morrish and K.H. Haneda: *J. Appl. Phys.*, 1981, vol. 52, pp. 2496–98.
36. J.M.D. Coey: *Phys. Rev. Lett.*, 1971, vol. 27, pp. 1140–42.
37. A.E. Berkowitz, J.A. Lahut, I.S. Jacobs, L.M. Levinson, and D.W. Forester: *Phys. Rev. Lett.*, 1975, vol. 34, pp. 594–97.
38. A.E. Berkowitz, J.A. Lahut, and C.E. VanBuren: *IEEE Trans. Magn. Mag.*, 1980, vol. 16, pp. 184–90.
39. J. Jacob and M.A. Khadar: *J. Appl. Phys.*, 2010, vol. 107, pp. 114310-1–10.